Bioactive Materials 16 (2022) 149–161

Contents lists available at ScienceDirect

Bioactive Materials

journal homepage: www.keaipublishing.com/en/journals/bioactive-materials

Crimped nanofiber scaffold mimicking tendon-to-bone interface for fatty-infiltrated massive rotator cuff repair

Liren Wang [a,b,1], Tonghe Zhu [a,1], Yuhao Kang [a,b], Jianguang Zhang [c], Juan Du [d], Haihan Gao [d,e], Sihao Chen [d], Jia Jiang [a,f,**], Jinzhong Zhao [a,f,*]

[a] Department of Sports Medicine, Department of Orthopedics, Shanghai Institute of Microsurgery on Extremities, Shanghai Jiao Tong University Affiliated Sixth People's Hospital, No. 600 Yishan Road, Shanghai, 200233, China
[b] Regenerative Sports Medicine and Translational Youth Science and Technology Innovation Workroom, Shanghai Jiao Tong University School of Medicine, No. 227 South Chongqing Road, Shanghai, 200025, China
[c] Department of Medgen Group Research Laboratory, 18 Qinglan 3 Rd, Shenzhen, 518118, China
[d] Biofunctional Materials Research Group, College of Chemistry and Chemical Engineering, Multidisciplinary Center for Advanced Materials, Institute of Advanced Studies, Shanghai University of Engineering Science, No. 333 Longteng Rd, Shanghai, 201620, China
[e] Shanghai Jiao Tong University School of Medicine, No. 227 South Chongqing Road, Shanghai, 200025, China
[f] Regenerative Sports Medicine Lab of the Institute of Microsurgery on Extremities, Shanghai Jiao Tong University Affiliated Sixth People' Hospital, No. 600 Yishan Road, Shanghai, 200233, China

ARTICLE INFO

Keywords:
Massive rotator cuff tear
Fatty infiltration
Nanofiber scaffold
Crimped structure
Tendon-to-bone interface

ABSTRACT

Electrospun fibers, with proven ability to promote tissue regeneration, are widely being explored for rotator cuff repairing. However, without post treatment, the microstructure of the electrospun scaffold is vastly different from that of natural extracellular matrix (ECM). Moreover, during mechanical loading, the nanofibers slip that hampers the proliferation and differentiation of migrating stem cells. Here, electrospun nanofiber scaffolds, with crimped nanofibers and welded joints to biomimic the intricate natural microstructure of tendon-to-bone insertion, were prepared using poly(ester-urethane)urea and gelatin via electrospinning and double cross-linking by a multi-bonding network densification strategy. The crimped nanofiber scaffold (CNS) features bionic tensile stress and induces chondrogenic differentiation, laying credible basis for *in vivo* experimentation. After repairing a rabbit massive rotator cuff tear using a CNS for 3 months, the continuous translational tendon-to-bone interface was fully regenerated, and fatty infiltration was simultaneously inhibited. Instead of micro-CT, μCT was employed to visualize the integrity and intricateness of the three-dimensional microstructure of the CNS-induced-healed tendon-to-bone interface at an ultra-high resolution of less than 1 μm. This study sheds light on the correlation between nanofiber post treatment and massive rotator cuff repair and provides a general strategy for crimped nanofiber preparation and tendon-to-bone interface imaging characterization.

1. Introduction

Rotator cuff tear (RCT), a frequent musculoskeletal disorder encountered by the healthcare system, is estimated to affect more than 20.7% of individuals aged 22–87 years; the lifetime societal costs related to RCTs has exceeded $3.44 billion in the United States alone [1,2]. However, 10–40% of the patients with RCTs inevitably develop massive RCTs (MRCTs) with mild or severe fatty infiltration in the rotator cuff muscle, resulting in persistent pain or pseudo-paralysis [3–5]. The issue of fatty-infiltrated MRCT (fi-MRCT) requires an urgent solution, as current treatments are ineffective and the failure rate of surgery ranges from 62 to 95% [6–10]. The challenges of tendon-to-bone interface

Peer review under responsibility of KeAi Communications Co., Ltd.
* Corresponding author. Department of Sports Medicine, Department of Orthopedics, Shanghai Institute of Microsurgery on Extremities, Shanghai Jiao Tong University Affiliated Sixth People's Hospital, No. 600 Yishan Road, Shanghai, 200233, China.
** Corresponding author. Department of Sports Medicine, Department of Orthopedics, Shanghai Institute of Microsurgery on Extremities, Shanghai Jiao Tong University Affiliated Sixth People's Hospital, No. 600 Yishan Road, Shanghai, 200233, China.
E-mail addresses: jessicajj19@hotmail.com (J. Jiang), jzzhao@sjtu.edu.cn (J. Zhao).
[1] These authors contributed equally to this work.

https://doi.org/10.1016/j.bioactmat.2022.01.031
Received 19 September 2021; Received in revised form 16 January 2022; Accepted 17 January 2022
Available online 25 January 2022

regeneration and muscle fat infiltration render difficulties in fi-MRCT repair.

To address the problem of repairing fi-MRCTs, tissue-engineered electrospun scaffolds have been proposed as a potential approach [11–13]. To date, the reported electrospun scaffolds used for RCTs all consisted of smooth, unconnected nanofibers, and the most common strategy of promoting tendon-to-bone interface recovery is adding chondrogenic or osteogenic factors, with little attention paid to the nanofibers themselves [14,15]. Without any post treatment, the smooth, unconnected nanofibers usually slip resulting in scaffold deformation, which would subsequently hinder the regeneration procedure. Welding the nanofibers at their cross points might effectively prevent deformation [16–18]. Thus, the implanted scaffold should match the *in situ* microstructure of the specific tissues being regenerated, which might better support the regeneration procedure. Su et al. reported that the microstructure of bone tissue is porous, whereas tendon tissue is composed of dense and crimped nanofibers [19]. The critical role of this crimped microstructure should be emphasized in electrospun scaffolds used for tendon repair, as it mechanically and morphologically mimics natural tendon tissues, and can promote the proliferation of tendon cells [20–22]. To date, the morphology of the nanofibers in electrospun scaffolds used for rotator cuff repair has not been emphasized. Therefore, we hypothesized that modifying the nanofiber morphology to mimic the tendon-to-bone interface may promote the suitability of scaffolds for tendon-to-bone regeneration, compared to the previously reported untreated nanofiber scaffolds.

Not only is the relationship between nanofiber morphology and tendon-to-bone interface regeneration uncertain, but the characterization of tendon-to-bone interface healing has not yet been determined. Histological evaluations, including Safranin O/Fast Green and immunohistochemical staining, are the common characterizations for tendon-to-bone interface healing. However, sections of tendon-to-bone interface can only be used to evaluate differences in the protein composition after healing, while the 3D structure of the tendon-to-bone interface, which is just as important as the protein composition, is lost. Although Rossetti et al. has successfully used μCT to visualize the microstructure of the native tendon-to-bone interface, no study considering the microstructure of tendon-to-bone interface healing has yet been reported [23]. Research on tissue engineering scaffolds for MRCT mainly uses micro-computed tomography (micro-CT) to evaluate the footprint of the rotator cuff healing site [24–26]. The resolution of micro-CT is relatively low and can only be used to analysis differences in bone volume after repair. Unlike bone volume recovery, the healing of the continuity and microstructure of the tendon-to-bone interface is a central parameter in tendon-to-bone interface regeneration, and a spatial evaluation of tendon-to-bone interface on the transition region spanning ~300 μm induced by tissue engineering scaffolds is under great need while yet unachieved. Thus, we speculated that visualizing the 3D microstructure of the tendon-to-bone interface is a more direct and highly accurate method for evaluating tendon-to-bone interface regeneration, compared with the previously reported strategies.

Given the abovementioned circumstances, we aimed to (1) fabricate a bionic nanofiber scaffold mimicking the microstructure of the tendon-to-bone interface using a general strategy and (2) assess its application *in vivo* to facilitate rotator cuff repair by evaluating the microstructure of the regenerating tendon tissue. Herein, we fine-tuned the nanofiber morphology of our previously reported poly(ester-urethane)urea (PEUU) gelatin-incorporating nanofibers to prepare an electrospun nanofiber scaffold via double crosslinking (Scheme 1). We used a multi-bonding network densification strategy, with a crimped microstructure,

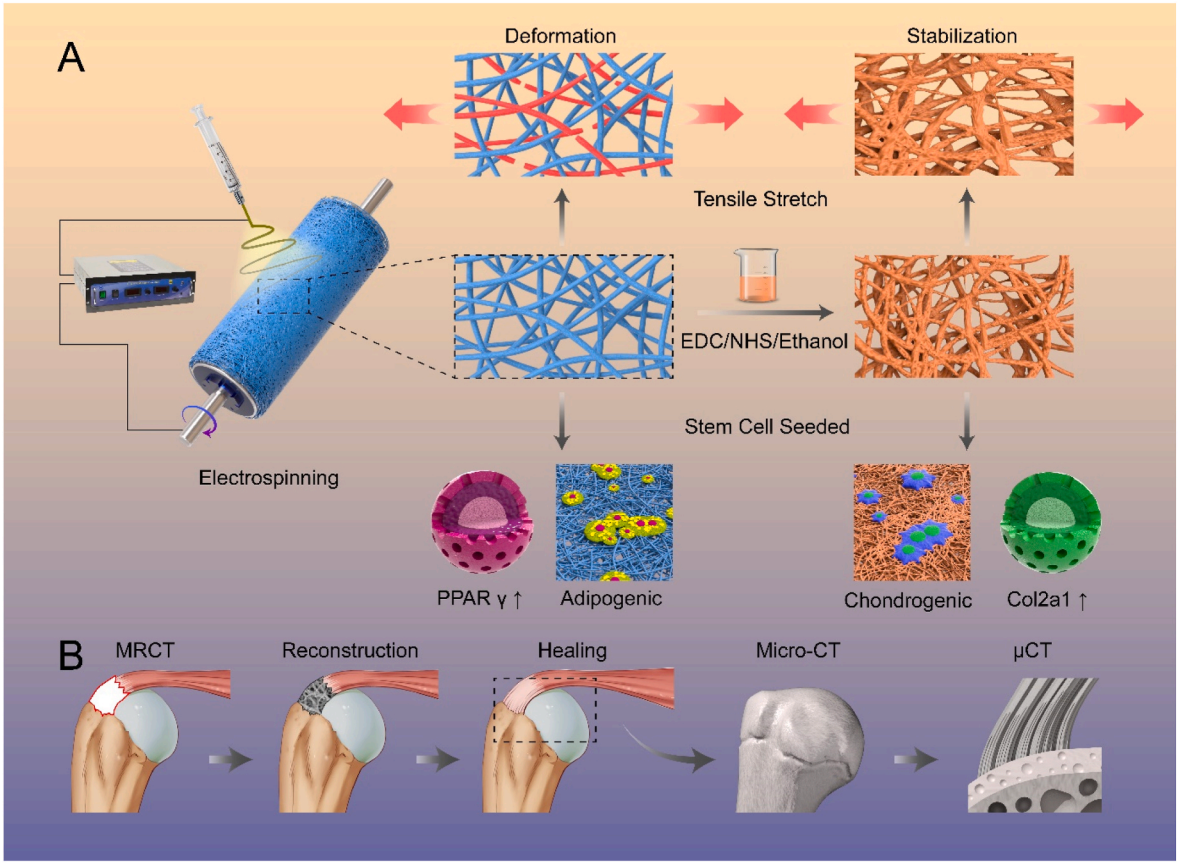

Scheme 1. Schemata of fabrication of the crimped nanofibrous scaffold for massive rotator cuff tear repairing. (A) Fabricated crimped nanofibrous scaffold can better resist the tensile stretch and promote chondrogenic induction; (B) μ-CT can directly visualize the tendon-to-bone interface induced by crimped nanofibrous scaffold.

for biomimicking the native tendon-to-bone interface ECM both biomechanically and biologically [25]. We further explored whether the heterogeneous microstructural response can mediate stem cell directional differentiation *in vitro*. Next, an optimally modified crimped scaffold was used for *in vivo* fi-MRCT repairing. The actual healing microstructure of the tendon-to-bone interface at a resolution of less than 1 μm was visualized, and recovery of the continuity of the transitional structure induced by the crimped nanofibers with a spatial perspective was confirmed. This study provides a general strategy for crimped nanofiber scaffold synthetization designed for fi-MRCT repair and direct tendon-to-bone interface imaging characterization.

2. Materials and methods

2.1. Materials

With a butanediamine chain extension, 1,6-hexamethylene diisocyanate and polycaprolactone diol (HO–PCL–OH) were used to synthesize PEUU, according to a previous study [27]. The average molecular weight of the synthesized PEUU was estimated to be 1.5×10^5.

2.2. Fabrication of nanofiber scaffold (NS)

NS was prepared using the electrospinning process. Briefly, 10% w/v solution from a blend of PEUU and gelatin (Sigma-Aldrich Chemical Reagent Co., Ltd., St. Louis, MO, USA) (75:25) was dissolved in 1,1,1,3,3,3-hexafluoro-2-propanol (Shanghai Darui Fine Chemical Co., Ltd., Shanghai, China). Located 12 cm away from aluminum foil, the clarified compound solution was fed at 1.0 mL/h at +10 kV. The electrospinning process was performed at room temperature (25 °C).

2.3. Crosslinking of NS

(NHS)-crosslinked NS nanofiber scaffolds were prepared as follows. A homogeneous solution of 200 mL of 90% ethanol, EDC (0.70 g), and NHS (0.30 g) was prepared. Thereafter, 2 cm × 2 cm × 0.5 cm NSs were immersed in the prepared crosslinking solution for 3 h (CNS1), 12 h (CNS2), or 24 h (CNS3) at room temperature. Subsequently, each scaffold was washed three times in triple-distilled water at 25 °C and freeze-dried for further utilization.

2.4. Characterization and performance testing of scaffolds

The micro-nano structure of each nanofiber scaffold was observed by scanning electron microscopy (NOVA NanoSEM 230, Long Island, NY, USA). The mechanical properties of the scaffolds were investigated using a material testing machine (H5K-S; Hounsfield, Redhill, UK) with a crosshead speed of 1 mm/min under a load of 200 N, according to the method ASTM D638-98 (n = 9). The surface topography of NS and CNS3 were evaluated using an Olympus OLS5000 (Zeiss-material type, Germany). The details of the chemical composition, average pore diameter, porosity, wettability, and dynamic mechanical analysis (DMA) of the scaffolds are listed in the Supporting *Information.*

2.5. Bone marrow stem cell (BMSC) proliferation assay

NS, CNS1, CNS2, and CNS3 were first immersed in 75% alcohol for 15 min for disinfection. After carefully washing the scaffolds three times in phosphate-buffered saline (PBS), each scaffold (n = 3, φ = 14 mm) was placed in a 24-well plate and immersed in culture medium for 4 h. After refreshing the culture medium, 5.0×10^4 BMSCs were seeded on each scaffold for the proliferation assays. The morphology and viability of the cells on NS, CNS1, CNS2, and CNS3 were assessed using scanning electron microscopy (SEM) and Cell Counting Kit-8 assays, as previously described [25].

Chondrogenic Induction: NS, CNS1, CNS2, and CNS3 were seeded in the wells of six-well tissue culture plates for immunofluorescent staining and reverse transcription polymerase chain reaction (RT-qPCR) analyses, after pretreatment as previously described (n = 6 per group). We seeded 1.0×10^7 BMSCs on each scaffold and cultured them with chondrogenic differentiation medium for 14 d. After 14 d of chondrogenic differentiation, each scaffold was washed three times with PBS. The experimental details of the immunofluorescent staining of collagen II and RT-qPCR are provided in the Supporting *Information.*

2.6. Adipogenic induction

3T3-L1 cells were used to assess adipogenic differentiation, as previously described [25]. NS, CNS1, CNS2, and CNS3 were seeded into separate wells of 24-well plates and pretreated as previously described (n = 6 per group). 3T3-L1 cells were seeded at a density of 5.0×10^5 cells/well and cultured with adipogenic differentiation medium for 8 d. After 8 d of culture induction, the 3T3-L1 cells were subjected to immunofluorescent and oil red O staining (Solarbio, Beijing, China). Details of the immunofluorescent staining of PPARγ and oil red O staining are provided in the Supporting *Information.*

2.7. Rabbit MRCT reconstruction

All surgical procedures were performed on rabbits according to the policies of the Institutional Animal Care and Use Committee of Shanghai Jiao Tong University affiliated Shanghai Sixth People's Hospital. Animal experiments were approved by the Animal Welfare Ethics Committee of Shanghai Sixth People's Hospital.

Sixty-eight mature male New Zealand rabbits weighing 2.6 ± 0.2 kg were used in the current study and were randomly divided into defect (n = 17), autograft reconstruction (n = 15), NS (n = 15), CNS3 (n = 17), and normal (n = 4) groups. The rabbits were anesthetized with 3% pentobarbital sodium. Both shoulders of the rabbits were carefully shaved and sterilized. The rotator cuff was exposed through gradual incision of the skin and the deltoid muscle. A 1.0 cm × 0.5-cm rotator cuff tendon defect, including the supraspinatus, infraspinatus, and subscapularis tendons, was made on the footprint of the rotator cuff tendon and the cartilage at the footprint site was further destroyed using a No. 15 blade knife. For the defect group, the supraspinatus tendon defect was left untreated. For the autograft reconstruction group, the tensor fasciae latae muscle tendon was harvested to fill the tendon defect. Two 1.2-mm-diameter bone tunnels were made on the footprint of the rotator cuff. The distal site of the autograft was fixed to the footprint of the rotator cuff by cross suture through two bone tunnels using No 2-0 nylon sutures and the proximal site of the autograft was tied to the remaining rotator cuff tissue also using No 2-0 nylon sutures. For the NS and CNS3 groups, the defects were subsequently refilled with NS or CNS3, respectively (Fig. S1). Postoperative activity was not restricted. One and three months after surgery, five rabbits from each group were used for micro-CT and histological assessments of the rotator cuffs. Additional testing details are available in the Supporting *Information*.

2.8. X-ray microscope evaluation

Four rotator cuff tendon–humerus complexes from the defect and CNS3 group (3 months after implantation) and normal group were evaluated by X-ray microscopy. Each complex was cut into cubes of 5 mm per edge with a dental drill and fixed in 4% paraformaldehyde for 48 h. After washing in double-distilled water for 5 h, the samples were transferred into Lugol's iodine solution for 48 h. The samples were then washed in 70% ethanol and stored in 100% ethanol before measurement. X-ray microscopic evaluation was performed using a Zeiss 520 Versa, with an optical magnification of 4 × . Projections (1,601) were measured after exposure for 3 s at 80 kV and 7 W. The defective voxel sizes of the rotator cuff tendon–humerus complexes were 8 and 0.7031

μm. CT acquisitions were reconstructed using the XMR Reconstructor software provided with the scanner, with manual center shift correction. Dragonfly (Object Research Systems, Montreal, Canada) was used for rendering.

2.9. Statistical analysis

All quantitative data are presented as mean ± standard error. Differences between groups were first analyzed using a one-way analysis of variance, with significance set to $P < 0.05$. When significant differences were detected, a post-hoc least significant difference test was performed to compare the two groups, with a significance level of $P < 0.05$.

3. Results

3.1. Characterization of nanofiber scaffolds

The fabrication and utilization of the nanofiber scaffolds (NS) and crimped nanofiber scaffolds (CNS) used via multi-bonding network densification strategy in this study are illustrated (Fig. 1A and B and S2) [28]. SEM images of the morphological and structural properties of NS, CNS1 (CNS immersed in the prepared crosslinking solution for 3 h), CNS2 (CNS immersed in the prepared crosslinking solution for 12 h), and CNS3 (CNS immersed in the prepared crosslinking solution for 24 h) are shown (Fig. 1C). With increasing reaction time between the fiber and solvent, the fibers wound around each other, and the shape of the scaffold changed from straight to twisted, gradually becoming more similar to the natural tendon-to-bone interface. However, over time, the reaction (nanofiber scaffold immersed in crosslinking solution for 48 h) results in excessive deformation of the nanofibers (Fig. S3). The electrospun scaffold with bound nanofiber, left little space for cell migration and proliferation, which is not suitable for tissue engineering; therefore, the scaffold was abandoned before further testing. As previously suggested, not only the morphology, but the mechanical properties of the scaffolds changed after crosslinking solution treatment [29]. The typical curves of NS, CNS1, CNS2, and CNS3 are presented (Fig. 1 D–G). It is apparent that, from NS to CNS3, the tensile stress, Young's modulus, and elongation at break were improved, and the tensile stress of CNS3 increased to 26.49 MPa, which is similar to that of natural tendon tissue. The mechanical property of CNS3 was remarkably increased compared to that of NS, which can be explained by two reasons. First, the free nanofibers got welded to each other during the crosslinking procedure, which subsequently increased the mechanical property of the scaffold [30]. Moreover, the ethanol treatment results in increased crystallinity of the nanofiber [20]. The fiber possibly crimps instead of the original straight morphology. During this procedure, energy is released and the whole scaffold can now endure higher mechanical stress compared with the original condition. In tissue engineering, the mechanical properties of scaffolds should be matched with the natural mechanical properties of a diverse range of tissues; otherwise, mismatched scaffolds may result in local hyperplasia or scar tissue formation. The fabricated scaffold CNS3 possessed similar structural and mechanical properties to the natural tendon-to-bone interface and might be a promising alternative option to induce tendon-to-bone interface regeneration.

The biomechanics of transplanted scaffolds are affected by characteristics of the local microenvironment, such as temperature and stretching. Therefore, we selected scaffolds in the wet state to investigate their stress–strain effects using DMA, as described previously [31]. After transplantation, the rotator cuff scaffold will experience repeated stretching under different elongation and stress conditions. Therefore, deformation of the scaffold should be limited to ensure correct shoulder function. DMA was used to evaluate the shape-memory capabilities of the scaffolds under different stress and temperature conditions. The deformation index, R_r, was calculated using Equation (1), where ε_{deform} is the deformed strain, ε_{final} is the final strain, and ε_{begin} is the initial strain.

$$R_r\,(\%) = \frac{\varepsilon_{deform} - \varepsilon_{final}}{\varepsilon_{deform} - \varepsilon_{begin}} \quad (1)$$

As NS can dissolve under the testing conditions, only CNS1, CNS2, and CNS3 were included in the DMA. The typical stress–-strain–temperature curves of CNS1, CNS2, and CNS3 are presented (Fig. 1H–K). The R_r values of CNS1, CNS2, and CNS3 were 71.67%, 74.07%, and 76.47%, respectively. The increasing R_r values of the DMA from CNS1 to CNS3 indicate that after exposure to stretching and temperature, the most irreversible deformation occurred in CNS1, while CNS3 provided the best mechanical support and the greatest resistance to deformation. The impressive shape-memory properties of CNS3 would help to prevent scaffold breakage soon after implantation.

The mean pore diameter, porosity, and surface hydrophilicity of scaffolds are critical parameters affecting tissue regeneration processes. As a crucial factor, the chemical structure of the materials affects the hydrophilicity of a scaffold. The crosslinking process was qualitatively evaluated by attenuated total reflection–Fourier transform infrared (ATR–FTIR) spectroscopy. The broad peak observed at 3500–3300 cm^{-1} represents the stretching vibration of O–H, which is abundant in the gelatin chain. The high intensity of the gelatin peak at 1570 cm^{-1} was mainly due to the high density of N–H bonds. There were no significant changes in the magnitudes of the peaks with crosslinking treatment after blending the gelatin with PEUU. This is likely due to the inclusion of several gelatin molecules in the NS and the high degree of overlap of the absorption peaks of the amide and ester groups in PEUU and gelatin (Fig. S4A). Gelatin, a hydrolyzed form of collagen, has some remaining crystalline segments of collagen, particularly at approximately 21.2° (Fig. S4B). However, the orientation of the gelatin and PEUU molecular chains during electrospinning also affects PEUU nanofiber crystallization. The wide-angle X-ray diffraction pattern of PEUU nanofibers showed that their crystallization was diffuse. In addition, the PEUU and NS curves were clearly analogous, which resulted from the small molecular chain glide during hybrid fabrication. During crosslinking treatment, crystal alignment was caused by the movement of the molecular chain.

Pure PEUU nanofiber scaffolds are hydrophobic, which is a disadvantage for cell spreading and proliferation. However, NSs have carboxyl, amino, or hydroxy groups on their surfaces, and therefore possess hydrophilic characteristics. The water contact angle was zero (Fig. S4C). The surface properties of the scaffolds are not only closely related to the microstructure of the fibers but are also associated with the different spatial conformations of the gelatin and PEUU molecules. Crosslinking decreased the size of the interfiber pores (Fig. S4D) and further decreased the porosity of CNS3 (Fig. S4E). We attributed these alterations to the superficial erosion of the fiber surface. The surface of CNS3 was rougher than that of NS. The Sq of the NS was 0.31 ± 0.45 μm and that of CNS3 was 0.58 ± 0.74 μm, suggesting that the crosslinking procedure and the reaction between the solvent and the fibers significantly changed the surface topography of each scaffold (Fig. 1L and M).

3.2. Biocompatibility, differentiation, and anti-adipogenesis in vitro

Stem cells were seeded onto the surface of the prepared scaffolds to evaluate the ability of the electrospun scaffolds to facilitate collagen II regeneration and inhibit adipogenic induction (Fig. 2A). The proliferation of rabbit BMSCs on the electrospun scaffolds was investigated to evaluate their cytocompatibility. Typical spindle morphologies and abundant lamellipodia were observed. Confluent BMSC colonies were observed over CNS3 on day 7 (Fig. S5). The absorbance index of the BMSCs seeded on CNS3 increased to 1.58 ± 0.01 by day 7. This was significantly higher than the absorbance indices of NS (1.15 ± 0.03), CNS1 (1.16 ± 0.03), and CNS2 (1.48 ± 0.03) (Fig. 2B). Thus, CNS3 significantly increased the proliferation of BMSCs compared with the other three scaffolds on day 7.

The expression of collagen II, as a representative protein at the

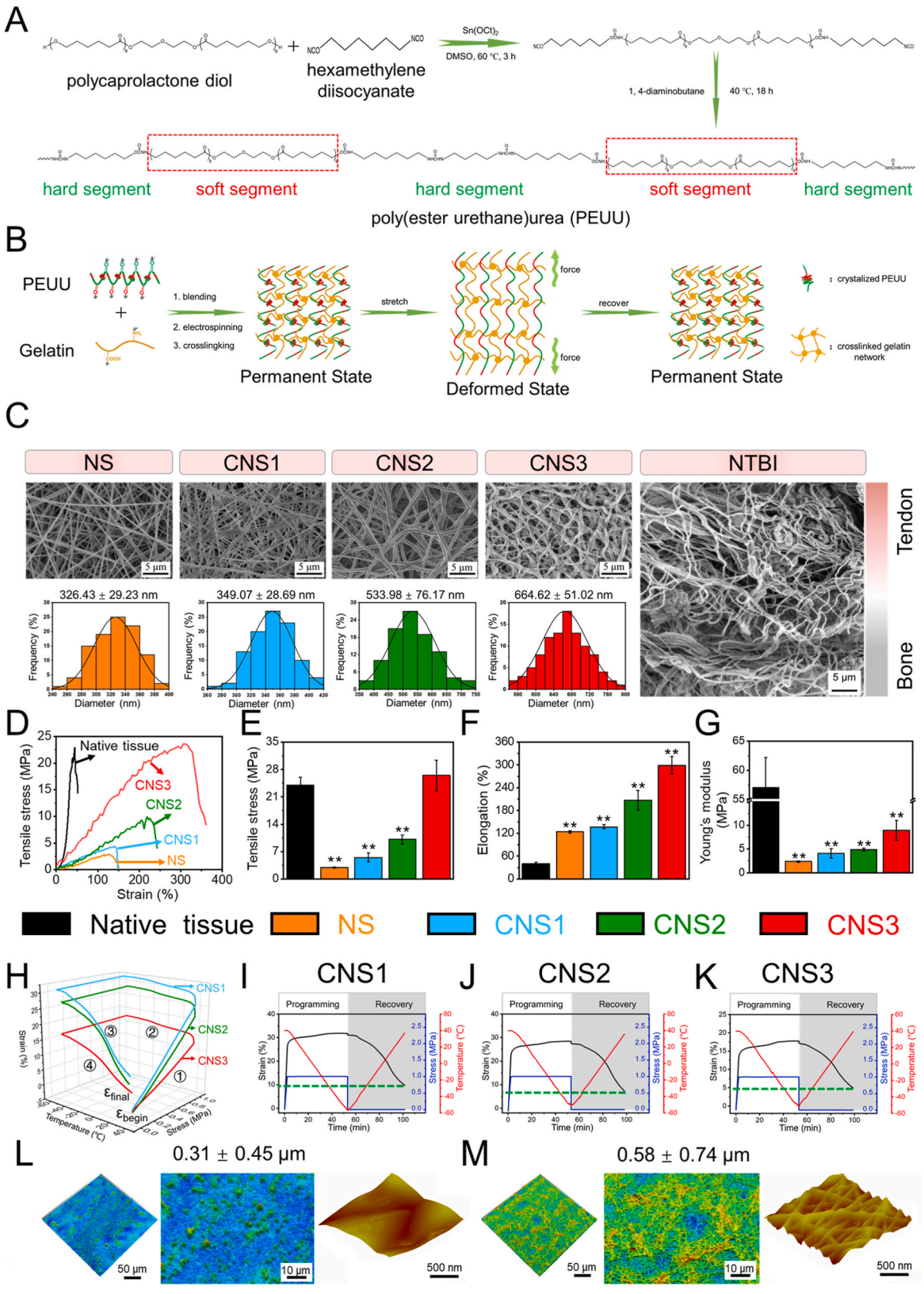

Fig. 1. Scanning electron microscopy images and mechanical testing of the scaffolds and natural tissue. (A) synthesis mechanism of PEUU, (B) self-fitting mechanism of the scaffolds; (C) Scanning electron microscopy images of NS, CNS1, CNS2, CNS3, and NTBI; (D–G) The mechanical characterization of native tendon tissue, NS, CNS1, CNS2, and CNS3; (H–K) Dynamic mechanical analysis of CNS1, CNS2, and CNS3. (L–M) Laser confocal microscopy and atomic force microscopy of NS and CNS3. *, significant difference compared with NS, $P < 0.05$; **, significant difference compared with NS, $P < 0.01$; NTBI, natural tendon-to-bone interface; NS, nanofiber scaffold; CNS, crimped nanofiber scaffold.

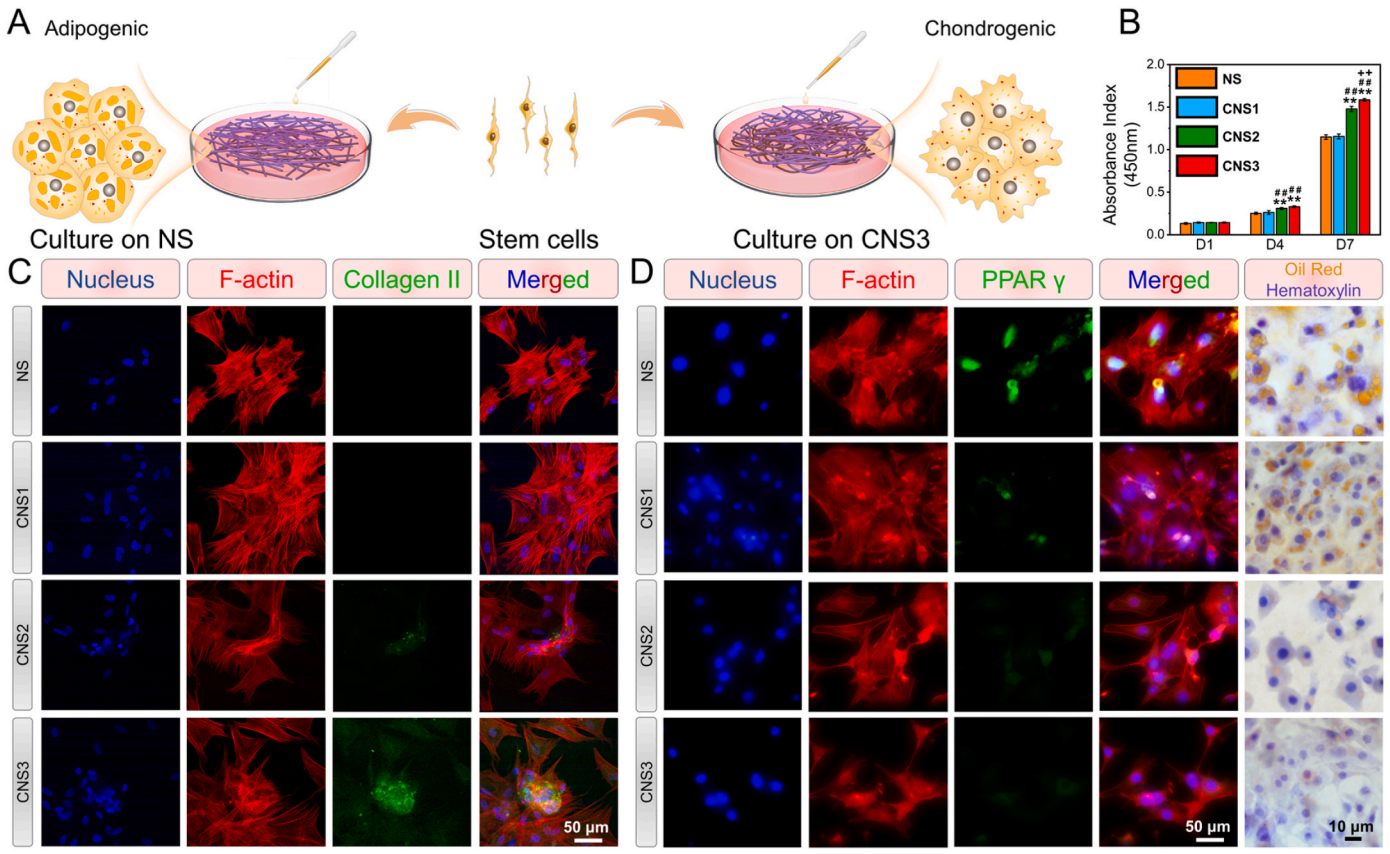

Fig. 2. Adipogenic and chondrogenic induction of cells on scaffolds. (A) Stem cells seeded on NS, CNS1, CNS2, or CNS3 for adipogenic and chondrogenic induction; (B) Proliferation assays of bone marrow stem cells (BMSCs) on the scaffolds on days 1, 4, and 7; (C) immunofluorescent staining of *col2a1* in BMSCs seeded on the scaffolds after 14 d of induction; (F) immunofluorescent staining of PPARγ and oil red O of 3T3-L1 cells seeded on the scaffolds after 14 d of induction. Significant difference compared with the NS (*), CNS1 ($^{+}$), and CNS2 ($^{\#}$) groups, $P < 0.05$; significant difference compared with the NS (**), CNS1 ($^{++}$), and CNS2 ($^{\#\#}$) groups, $P < 0.01$; NS, nanofiber scaffold; CNS, crimped nanofiber scaffold.

tendon-to-bone interface, was evaluated by immunofluorescence staining (Fig. 2C). Collagen II was expressed significantly higher in the BMSCs seeded on CNS3 than in those seeded on the other scaffolds. Three marker genes, aggrecan, *col2a1*, and *sox9*, were selected to evaluate the chondrogenic ability of the BMSCs seeded on each scaffold. The expression of these genes was analyzed by RT-qPCR after 14 d of chondrogenic induction (Fig. S6). The expression of aggrecan was significantly higher in the BMSCs on CNS3 (4.50 ± 1.54) than in those on NS (0.92 ± 0.13). A similar increase in *col2a1* and *sox9* expression was observed after 14 d of chondrogenic induction. These results indicate that CNS3 markedly promoted chondrogenic gene expression *in vitro* compared with the other three scaffolds.

Significant fatty infiltration is observed in MRCTs, and this impairs shoulder function. The adipogenic differentiation of 3T3-L1 cells seeded on each scaffold was evaluated by oil red O staining and immunofluorescent staining of peroxisome proliferator-activated receptor gamma (PPARγ) (Fig. 3D). After 14 d of induction, numerous intracellular lipid droplets were observed in the 3T3-L1 cells seeded on NS, but the number and size of the lipid droplets in the 3T3-L1 cells on CNS3 were significantly decreased compared with NS (Fig. S7). Immunofluorescent staining indicated that PPARγ expression was considerably upregulated in the 3T3-L1 cells seeded on NS compared with those seeded on CNS3.

The mechanical properties of a scaffold are highly correlated with the differential direction of seeded stem cells [32–34]. On a soft scaffold, the weak mechanical connection between the scaffold and the stem cells leads to inhibited activation of F-actin complexes, finally resulting in adipogenic induction [35]. In contrast, strong mechanical feedback from a stiff scaffold increases cell tension, leading to chondrogenic induction [36]. Our results also suggest that the BMSCs on CNS3 were likely subjected to chondrogenic differentiation, while adipogenic differentiation was inhibited. Based on these findings, we concluded that CNS3 was more suitable than the other three scaffolds for rotator cuff regeneration.

3.3. Tendon-to-bone interface and tendon regeneration in situ

The torn rotator cuff tendon experiences continuous retraction and degeneration in patients with fi-MRCT and the remaining tendon tissues are generally too short to be directly sutured to the rotator cuff footprint. Thus, the difficulties in repairing fi-MRCTs lie not only in the regeneration of the tendon-to-bone interface and the inhibition of fatty infiltration into the muscle, but also in the regeneration of the tendon tissue connecting the tendon-to-bone interface. To stimulate this pathological state, a rabbit MRCT model was developed, in which most of the subscapularis, supraspinatus and infraspinatus tendons were removed from the tendinous insertion, leaving only a small amount of tendon tissue connecting the rotator cuff muscles. Peroneus longus tendon autografts, NS, and CNS3 were prepared for MRCT repair [37]. The tendon–humerus complexes were harvested 1 and 3 months after implantation for high-resolution micro-CT (Fig. 3A), Safranin O/Fast Green staining, immunohistochemistry, and transmission electron microscopy (TEM) evaluation.

One month after implantation, no significant differences in bone volume fraction (BV/TV) or trabecular number (Tb.N) were observed among the four groups (Fig. 3B–D). At 3 months, all three experimental groups presented significant increases in BV/TV and Tb.N compared with the defect group. The BV/TV and Tb.N of the CNS3 group increased by 59.48% ± 4.84% and 16.73% ± 1.33%, respectively, 3 months after

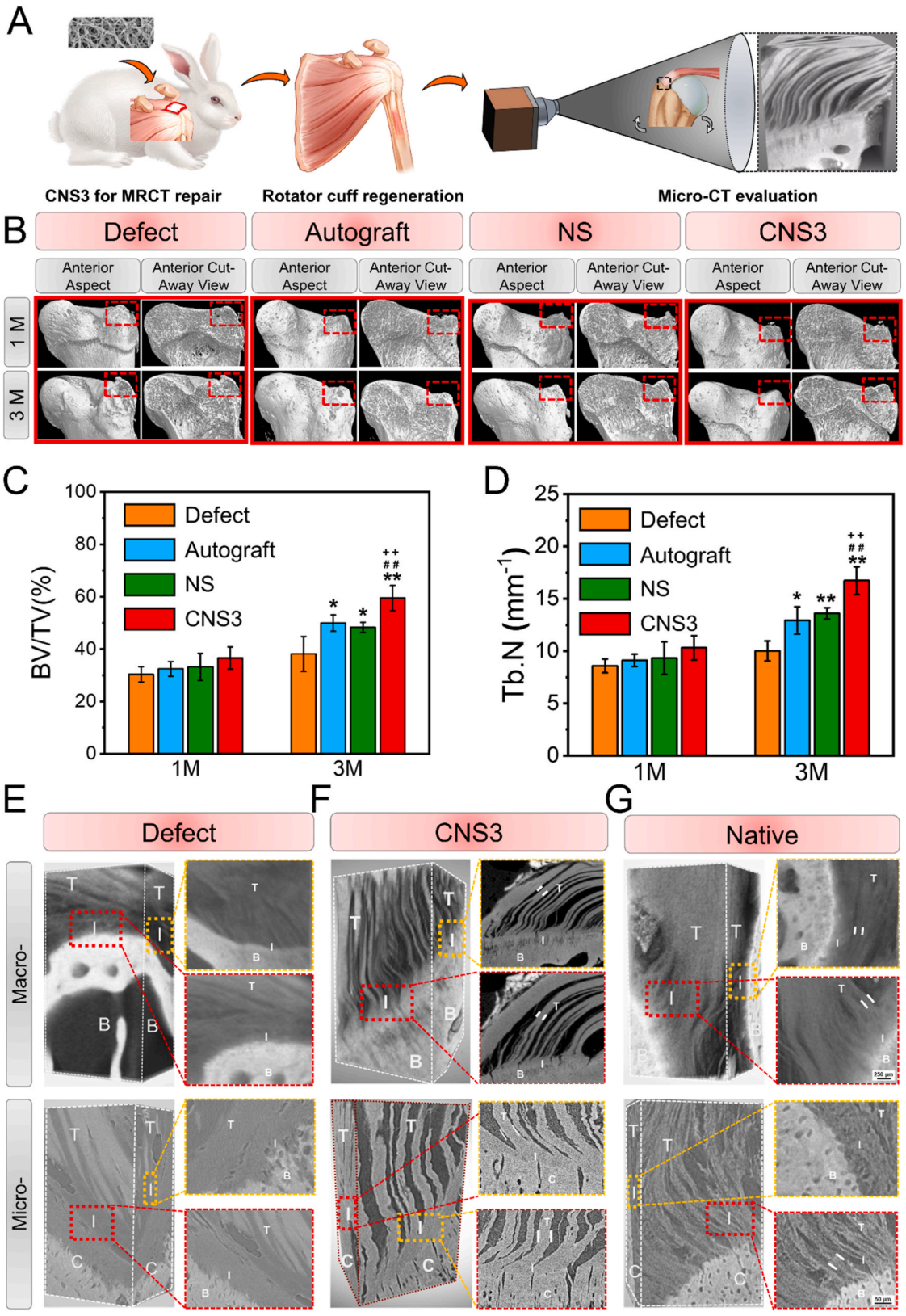

Fig. 3. Representative micro-computed tomography (micro-CT) images of the proximal humerus and quantitative analysis. (A) Schematic illustration of micro-CT for evaluating tendon-to-bone healing; (B–D) micro-CT images of the proximal humerus and quantitative analysis; (E–G): high-resolution micro-CT of the tendon-to-bone interface of the defect group at 3 M, CNS3 group at 3 M, and intact rotator cuff, with 8.5 μm (E) and 0.7 μm (F) resolutions. Significant difference compared with the defect (*), autograft ($^{+}$), and NS ($^{\#}$) groups, $P < 0.05$; Significant difference compared with the NS (**), CNS1 ($^{++}$), and CNS2 ($^{\#\#}$) groups, $P < 0.01$; B, bone; BV/TV, bone volume fraction; Tb.N, trabecular bone number; C, cartilage; CNS, crimped nanofiber scaffold; I, interface; NS, nanofiber scaffold; T, tendon.

surgery. CNS3 exhibited the greatest capability of inhibiting the loss of bone volume and degeneration of the trabecular bone structure.

High-resolution micro-CT was used to characterize the microstructure of the tendon-to-bone interface of the defect group at 3 M, CNS3 group at 3 M, and the intact rotator cuff. Micro-CT enabled the 3D reconstruction of the tendon-to-bone architecture, with resolutions of 8.50 and 0.70 μm, while preserving near-physiological conditions (Fig. 3E and F). Structural analyses using this imaging technique demonstrated that, after 3 months, the regenerative tissue over the tendon-to-bone interface was irregular and discontinuous, indicating the there was no chance of tendon-to-bone healing after fi-MRCT. The functioning of the tendon-to-bone interface would require healing. The damaged tendon-to-bone physiological structure cannot endure mechanical transduction from the scapula to the humerus, and this would result in re-tearing. Three months after CNS3 repair, the natural transition zone, where the tendon fibers unravel into thinner interface fibers before attaching to the bone, was fully recovered (Movie S1 and S2), laying a solid foundation for mechanical transduction. With resolutions of 0.70 μm, which has not been reported before, the connection between the tendon tissue and cartilage layer was achieved in the present study.

As shown by the results of the defect group, without adequate repairing, no sign of self-healing of the tendon-to-bone interface was observed. The interface was covered with irregular fiber tissue that cannot provide mechanical support for daily activities. In the CNS3 group, after 3 months of implantation, mature tendon fibers were induced by the nanofiber scaffold with a bionic microstructure. The parallel and regular fibers are essential for mechanical transduction. However, compared with the native tendon-to-bone interface, higher interface area between tendon fibers was observed in the CNS3 group, indicating that the induced tendon fibers do not have density similar to that of the native tendon tissue. A microstructure insertion maturing score was established according to the Tendon Maturing Score to evaluate the tendon-to-bone interface (Table S1 and Fig. S8). The observed mean diameters of the tendon and interface fibers were 126.77 ± 24.21 and 30.19 ± 7.02 μm, respectively in the CNS3-induced tendon-to-bone interface. The mean diameters of the tendon and interface fibers in the native tendon-to-bone interface were 183.10 ± 10.51 (P = 0.02) and 37.99 ± 2.06 μm (P = 0.14), respectively, suggesting that the regenerative tendon-to-bone interface was not as mature as the native structure. In future studies, bioactive factors could perhaps be added to promote the maturation of

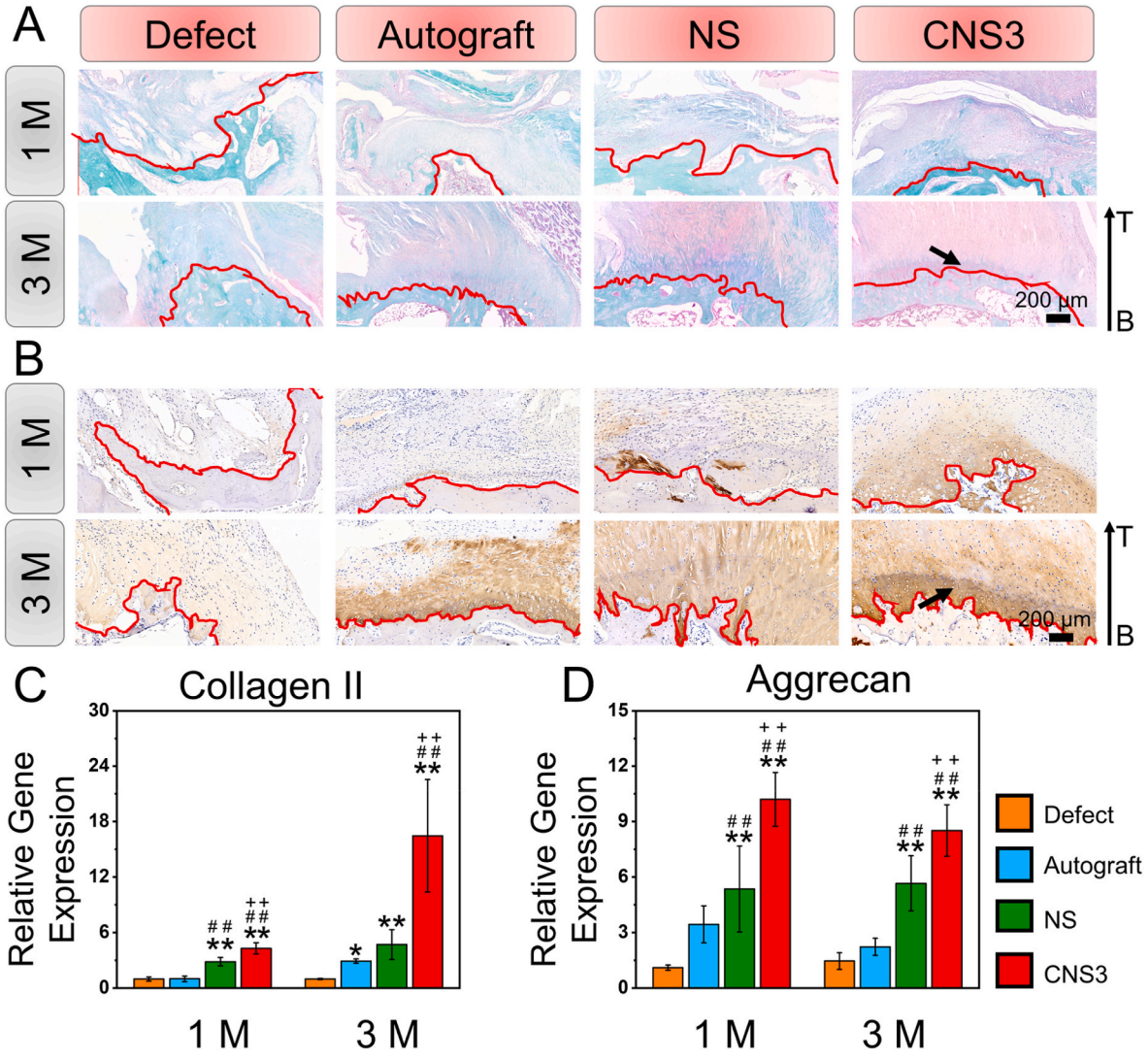

Fig. 4. Histological, immunohistochemical, and chondrogenic-related gene expression evaluation of tendon-to-bone regeneration. (A) Safranin O/Fast Green staining and (B) immunohistochemical staining of collagen II; (C–D) quantitative analysis of *in vivo* tendon-to-bone interface regeneration. Significant difference compared with the defect (*), autograft ($^{+}$), and NS ($^{\#}$) groups, $P < 0.05$; Significant difference compared with the NS (**), CNS1 ($^{++}$), and CNS2 ($^{\#\#}$) groups, $P < 0.01$; 1 M, 1 month; 3 M, 3 months; B, bone; CNS: crimped nanofiber scaffold; I, interface; NS, nanofiber scaffold; T, tendon. Red dotted shapes indicate the regenerated tendon-to-bone interface. Black arrows indicate collagen II expression.

the tendon-to-bone interface, and realize ideal healing conditions. The healing of the tendon-to-bone interface is the central issue in rotator cuff repairing. Previously, the tendon-to-bone interface was evaluated to mainly assess the regeneration of the cartilage layer, which functions as a mechanical transitional zone. However, a recent study reported that the transitional fibers on the interface may play a more important role in mechanical transduction. At the insertion site, tendon fibers comprised thinner fibers that helped endure not only longitudinal loading but also

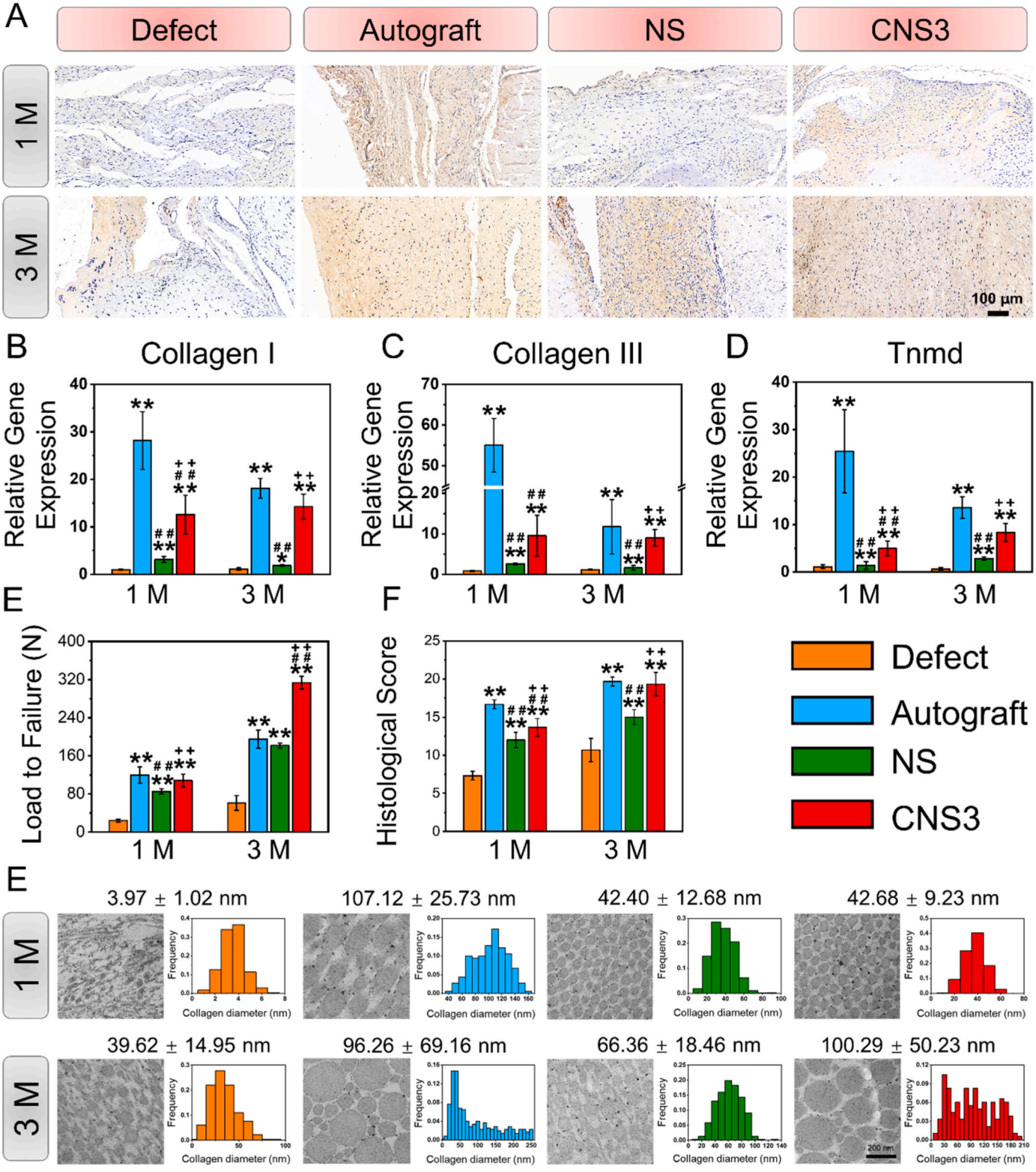

Fig. 5. Evaluation of tendon regeneration. (A) Immunohistochemical staining of collagen I; (B–D) tendon-related gene expression of regenerative tissue at 1 and 3 M; (E) representative TEM images and distribution of regenerative tendon tissue. Significant difference compared with the defect (*), autograft ($^{+}$), and NS ($^{\#}$) groups, $P < 0.05$; Significant difference compared with the NS (**), CNS1 ($^{++}$), and CNS2 ($^{\#\#}$) groups, $P < 0.01$; 1 M, 1 month; 3 M, 3 months; CNS, crimped nanofiber scaffold; NS, nanofiber scaffold; TEM, transmission electron microscopy; Tnmd, tenomodulin.

different angle-loading bearing. The recruited thinner tendon fibers decreased the mechanical mismatch between the tendon and the bone tissue and connected dissimilar materials.

Tendon-to-bone interface regeneration was further explored using histological and immunohistochemical evaluations according to previous study (Fig. 4A and B and S9, 10 and 11) [38]. H&E, Masson and Safranin O/Fast Green staining indicated that 1 month after implantation, a little cartilage was found in the defect group. Collagen II immunohistochemical staining also indicated that, although the collagen II regeneration level was relatively low among the four groups 1 month after surgery, the lowest collagen II expression was found in the defect group. Three months after implantation, a distinctive tidal line, indicating a mature tendon-to-bone interface, was observed in the CNS3 group. Moreover, immunohistochemical staining suggested that the collagen II level was significantly increased in the regenerative tendon-to-bone interface. The RT-qPCR results showed that the expression of chondrogenic genes, including collagen II and aggrecan, was significantly upregulated in the CNS3 group compared with that in the other three groups, 1 and 3 months after implantation (Fig. 4C and D). Thus, it can be inferred that CNS3 promoted chondrogenic gene expression, which subsequently facilitated tendon-to-bone healing.

Significant differences in collagen I regeneration and the relative gene expression levels in the tendons were found among the four groups. Immunohistochemical evaluation indicated that the autograft group had the highest collagen I expression after 1 month, whereas negligible collagen I regeneration was observed in the defect group (Fig. 5A). Moreover, the relative expression levels of collagen I, collagen III, and tenomodulin genes in the tendons were the highest in the autograft group after 1 month (Fig. 5B–D). Three months after surgery, collagen I expression was higher in the autograft and CNS3 groups than in the defect and NS groups, and the CNS3 group showed the highest collagen I expression in the tendons.

The ultrastructural morphology of regenerative collagen fibers was evaluated by TEM imaging (Fig. 5E). At 1 month, the collagen fibers (88.85 ± 2.93 nm) were markedly thicker in the autograft group than in the defect (37.20 ± 5.86 nm), NS (44.19 ± 4.03 nm), and CNS3 (47.58 ± 4.27 nm) groups. Three months after surgery, the average diameters of the collagen fibers in the autograft (104.15 ± 7.18 nm) and CNS3 (100.43 ± 6.82 nm) groups were significantly larger than those in the defect (40.72 ± 16.76 nm) and NS (67.01 ± 3.03 nm) groups.

The mechanical properties and tendon maturation scores of the regenerative rotator cuff tissues were investigated to evaluated *in vivo* regenerative effects. At 1 month, the load to failure and tendon maturation scores of the regenerative rotator cuff tissues in the defect group (24.13 ± 3.16 N, $P < 0.05$; 7.33 ± 0.58, $P < 0.05$) were significantly lower than those in the autograft (119.79 ± 16.88 N; 16.67 ± 0.58), NS (85.14 ± 5.62 N; 12.00 ± 1.00), and CNS3 groups (107.99 ± 13.84 N; 13.67 ± 1.15). Three months after surgery, the load to failure in the CNS3 group (313.58 ± 13.16 N) was higher than those in the defect (60.81 ± 15.41 N), autograft (194.99 ± 19.47 N), and NS (181.59 ± 5.01 N) groups, while the tendon maturation scores of the autograft (19.67 ± 0.58) and CNS3 (19.33 ± 1.53) groups were both significantly higher than those in the NS (15.00 ± 1.00) and defect (10.67 ± 1.53) groups.

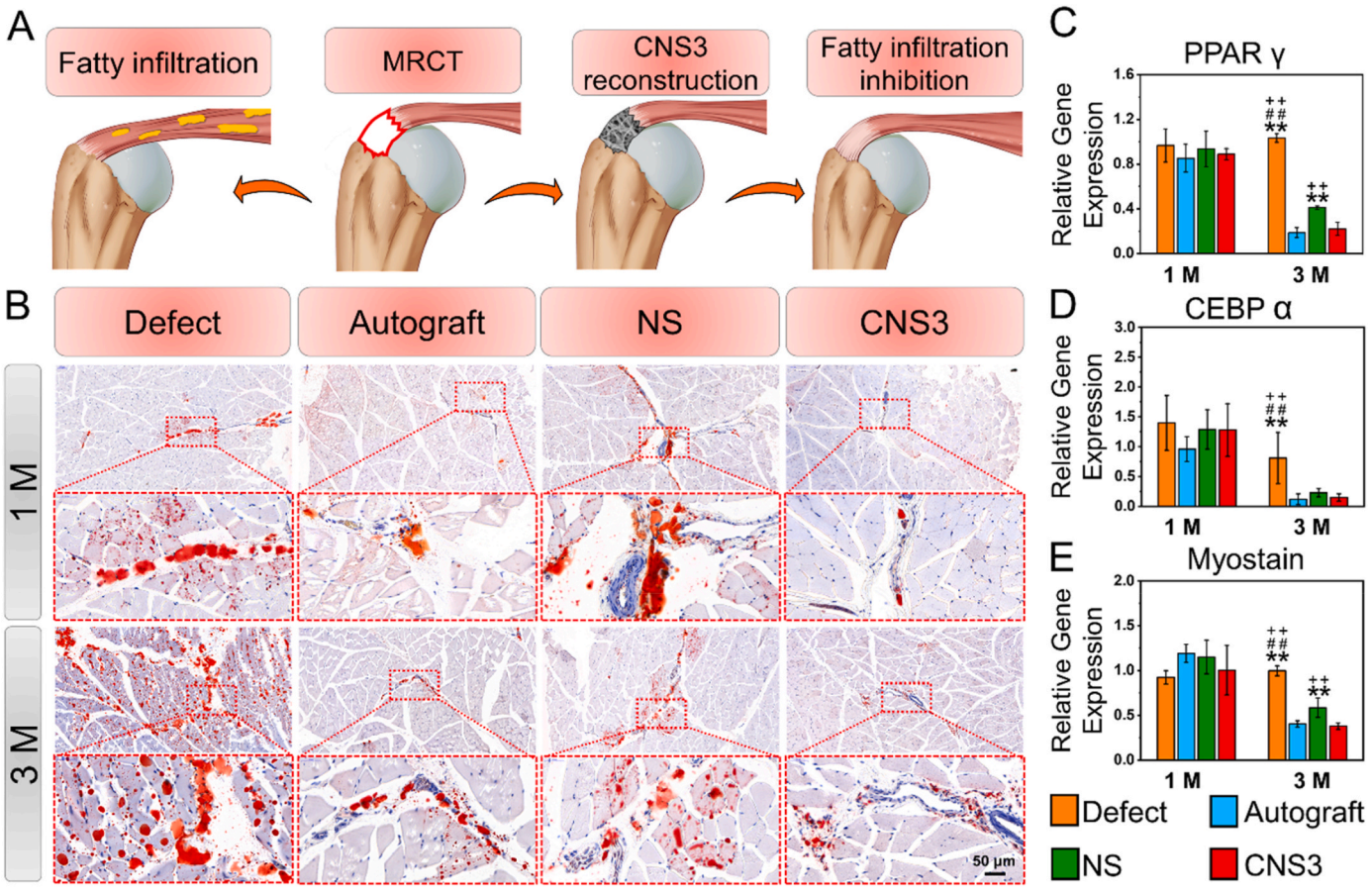

Fig. 6. Evaluation of fatty infiltration. (A) Representative oil red O images of rotator cuff muscle; (B) schematic illustration of CNS3 used for MRCT repair; (C–E) adipogenic-related gene expression in the supraspinatus tendon. Significant difference compared with the defect (*), autograft ($^{+}$), and NS ($^{\#}$) groups, $P < 0.05$; Significant difference compared with the NS (**), CNS1 ($^{++}$), and CNS2 ($^{\#\#}$) groups, $P < 0.01$; MRCT, massive rotator cuff tear; CNS, crimped nanofiber scaffold; NS, nanofiber scaffold.

3.4. Fatty infiltration inhibition in situ

The creation of MRCT resulted in fatty infiltration (Fig. S12) and one month after surgery, no significant differences in the oil red O staining area ratio or the maximum diameter or number of lipid droplets were found among the groups (Fig. 6). Additionally, the relative expressions of genes involved in fatty infiltration, including PPARγ, CCAAT enhancer-binding protein alpha, and myostatin, in the supraspinatus tendon were also similar among the groups. Three months after surgery, significant increases in the maximum diameter (85.97 ± 9.35 μm) and number (521.33 ± 124.91) of lipid droplets, the oil red O staining area ratio (8.59 ± 0.63%), and fatty infiltration-related gene expression levels were observed in the defect group compared with the CNS3 group. However, the values for these parameters decreased in both the autograft and CNS3 groups, indicating that both the native tendon autograft and the scaffold mimicking the mechanical properties and microstructure of native tendon tissue effectively inhibited fatty infiltration and promoted fi-MRCT repair.

4. Discussion

This study emphasizes the critical importance for tendon-to-bone healing of a crimped microstructure in electrospun scaffolds, a topic which has been previously overlooked in RCT repair. The crimped microstructure, mimicking the natural tendon-to-bone interface ECM, promoted chondrogenesis at the interface site, which subsequently facilitated the repair of fi-MRCT. Furthermore, previously reported rotator cuff repair studies lack a direct imaging technique to evaluate tendon-to-bone healing, instead evaluating bone volume at the footprint site of the rotator cuff by micro-CT, which can only be used to indirectly infer the tendon-to-bone interface. In this study, the continuity of the healed tendon-to-bone interface was directly visualized in 3D at a resolution of less than 1 μm, which has not been achieved previously. The direct visualization of the tendon-to-bone interface offers a straightforward method toward assessing healing effects. This work provides general strategy for crimped nanofiber preparation designed for fi-MRCT repairing and tendon-to-bone interface imaging characterization.

Without post treatment, the nanofibers of electrospun scaffolds can be disconnected, and during stretching, the general structure of the scaffold can destructive deformation owing to slippage between the nanofibers [39]. Thus, the importance of post treatment has been emphasized. Liu et al. found that, after ethanol treatment, there was an immediate energy release from straight nanofibers, which subsequently retracted the fibers and resulted in a crimped morphology. The treated electrospun scaffolds were equipped with this tendentious mechanical property [29]. However, with the increasing number of electrospun scaffolds fabricated for tendon-to-bone interface repair, the modification of the nanofibers has gained little attention as yet [40–42]. In this study, the importance of a crimped nanofiber microstructure was first mentioned in relation to tendon-to-bone interface repair. We found that the prepared crimped nanofiber scaffolds not only mechanically matched the native tendon tissue, as previously suggested, but were also biologically suitable for tendon-to-bone interface regeneration, promoting chondrogenesis. This could be attributed to the alternated morphology of the nanofiber scaffold. Using a laser confocal scanning microscope and atomic force microscope, we found that the roughness of the crimped nanofiber scaffold was increased compared with that of the smooth straight nanofiber scaffold, providing a suitable microenvironment for chondrogenic induction. Surface roughness is an important structural factor in directing stem cell differentiation. It facilitates focal attachments between the seeded cells and the rough scaffold; subsequently, it contributes to an increase in cartilage matrix formation [43,44]. Our *in vitro* stem cell differentiation results also confirmed that collagen II expression was increased and adipogenic expression was inhibited by the crimped nanofiber scaffold, laying the critical biological foundation for the *in vivo* experiment. The current findings suggest that, for electrospun scaffolds prepared for tendon-to-bone healing, the importance of a crimped microstructure should not be ignored.

To date, imaging, histology, and molecular biology are the common assessment methods for the tendon-to-bone interface, while imaging techniques are relatively immature. Although Rossetti et al. described the microstructure of the normal native tendon-to-bone interface, the microstructure of this interface after healing has not been investigated [23]. Owing to the limited resolution of micro-CT, most tendon-to-bone interface repair evaluations use micro-CT to assess changes in bone volume after repair to indirectly reflect tendon-to-bone interface healing [26,45,46]. However, bone volume loss is commonly caused by mechanical unloading after tendon tearing, and could potentially be effectively reversed by scaffold augmentation; tendon-to-bone interface healing is a completely different aspect of evaluation [47,48]. Ideal tendon-to-bone healing not only requires the regeneration of four transitional zones, including the tendon, fibrocartilage, mineralized fibrocartilage, and bone, but also requires the spatial restoration of the tendon-to-bone interface [49,50]. In a natural tendon-to-bone interface, a decreasing trend in tendon fiber diameter was observed, guaranteeing the mechanical loading capability of the tendon-to-bone interface, which connects two significant tensile modulus materials. Without the visualization of this unique structure, it is inappropriate to evaluate the healing effect. The microstructures of unhealed and healed tendon-to-bone interfaces were first reported in this study. Without repair, the fiber over the rotator cuff footprint is irregular and disconnected, while the tendon fibers induced by the crimped scaffold retained their continuity and naturally decreasing fiber diameter trends until their cartilage attachment points. Furthermore, the resolution of previously visualized tendon-to-bone interface microstructures was not small enough to observed the thinnest tendon-to-bone insertion structures, and SEM was used. However, like in histological evaluations, the 3D structure of the tendon-to-bone interface was lost in SEM observation. In this study, a resolution of less than 1 μm was achieved and a clear observation of the thinnest tendon-to-bone insertion structures was presented. These observations highlight the indispensable characteristics of μCT for subsequent studies evaluating tendon-to-bone healing.

As suggested by previous studies, the loss of bone begins immediately after the tearing of a tendon, presumably owing to the loss of mechanical loading [48]. The reconstruction of a torn rotator cuff using a crosslinked scaffold restores the mechanical transduction between the scapula and the humeral head, thus preventing subsequent bone loss in the footprint of the rotator cuff. Furthermore, the mechanical properties of crosslinked scaffolds were significantly improved compared with those of non-crosslinked scaffolds [51,52]. As suggested, the osteogenic induction of osteoblasts was increased on the stiff scaffolds and more bone matrix was generated at the defect site [53–55]. Tendon defects and fatty infiltration of the muscle contribute to poorer outcomes for fi-MRCTs than for smaller RCTs. Tendon defects are commonly observed in MRCTs. Scaffolds can promote tendon regeneration, and tendon-to-bone healing has clinical importance. By seeding annulus-fibrosus-derived stem cells, previous studies have shown that stiff scaffolds promote greater cell proliferation and cell spreading than soft scaffolds and show upregulated tendon-related gene expression [56]. In the current study, we also found that tendon-related gene expression was upregulated in CNS3 compared with that in NS *in vivo*. Moreover, 3 months after implantation, the tendons induced by CNS3 were not significantly different from autograft tendons with regard to maturing score, collagen I expression, and fiber diameter distribution. This may be explained by the fact that the crimped nanofiber structure is more similar to native tendon-to-bone tissue than smooth, straight fibers. After RCT, the process of fatty infiltration of the muscle is activated owing to the lack of mechanical loading, which substantially influences the outcome of rotator cuff repair. Previous studies have suggested that fatty infiltration is mediated by adipogenic differentiation [57–60]. Thus, scaffolds that inhibit adipogenic differentiation *in vitro* and *in vivo* should be ideal for RCT repair. Ye et al. suggested that, through F-actin

bundles, cells seeded on a stiff matrix are under more tension from focal adhesion and less likely to differentiate into fatty tissue [61]. In our *in vitro* and *in vivo* experiments, fewer and smaller lipid droplets were observed in CNS3 than in the other scaffolds. Additionally, adipogenic and myostatin gene expression was lower in CNS3.

5. Conclusions

In this study, we optimized the synthesis of an electrospun scaffold with a crimped wielded nanofiber, which could effectively endure higher tensile stretch and dynamic mechanical testing. Stem cells seeded on the CNS3 scaffold *in vitro* showed increased chondrogenesis and decreased adipogenesis, thereby laying a biological foundation for the subsequent *in vivo* experimentation. Three months after *in vivo* massive rotator cuff repairing, CNS3 effectively induced a continuous translational interface between the tendon and the bone. Regeneration of tendon tissue and inhibition of muscle fatty infiltration were also observed after CNS3 reconstruction. Taken together, this study offers novel insights into the application of an electrospun scaffold fabricated for RCT repair, by providing a general template for crimped nanofiber scaffold preparation and tendon-to-bone interface imaging-based characterization.

CRediT authorship contribution statement

Liren Wang: Investigation, Methodology, Data curation, Formal analysis, Writing – original draft. **Tonghe Zhu:** Investigation, Methodology, Data curation, Formal analysis, Writing – original draft, Funding acquisition. **Yuhao Kang:** Investigation, Visualization, Formal analysis. **Jianguang Zhang:** Investigation, Formal analysis, Funding acquisition. **Juan Du:** Investigation, Formal analysis. **Haihan Gao:** Investigation, Formal analysis. **Sihao Chen:** Resources. **Jia Jiang:** Conceptualization, Supervision, Writing – review & editing, Project administration. **Jinzhong Zhao:** Funding acquisition, Conceptualization, Supervision, Writing – review & editing, Project administration.

Declaration of competing interest

The authors declare no competing financial interest.

Acknowledgments

L. Wang and T. Zhu contributed equally to this work. This work was supported by Instrumental Analysis Center of Shanghai Jiao Tong University. This work was supported by the National Natural Science Foundation of China [Grant No. 81902186, 81671920, 31972923, 81871753, 81772341], National Key Research and Development Program of China [Grant No. 2018YFC1106200, 2018YFC1106201, 2018YFC1106202], and Technology Support Project of Science and Technology Commission of Shanghai Municipality of China [Grant No. 19441901700, 19441901701, 19441901702, 18441902800].

Appendix A. Supplementary data

Supplementary data to this article can be found online at https://doi.org/10.1016/j.bioactmat.2022.01.031.

References

[1] A. Yamamoto, K. Takagishi, T. Osawa, T. Yanagawa, D. Nakajima, H. Shitara, et al., Prevalence and risk factors of a rotator cuff tear in the general population, J. Shoulder Elbow Surg. 19 (1) (2010) 116–120.
[2] R.C. Mather 3rd, L. Koenig, D. Acevedo, T.M. Dall, P. Gallo, A. Romeo, et al., The societal and economic value of rotator cuff repair, J. Bone. Joint. Surg. Am. 95 (22) (2013) 1993–2000.
[3] J.H. Oh, B.J. Jun, M.H. McGarry, T.Q. Lee, Does a critical rotator cuff tear stage exist?: a biomechanical study of rotator cuff tear progression in human cadaver shoulders, J. Bone. Joint. Surg. Am. 93 (22) (2011) 2100–2109.
[4] M.S. Rashid, C. Cooper, J. Cook, D. Cooper, S.G. Dakin, S. Snelling, et al., Increasing age and tear size reduce rotator cuff repair healing rate at 1 year, Acta Orthop. 88 (6) (2017) 606–611.
[5] J.J. Barry, D.A. Lansdown, S. Cheung, B.T. Feeley, C.B. Ma, The relationship between tear severity, fatty infiltration, and muscle atrophy in the supraspinatus, J. Shoulder Elbow Surg. 22 (1) (2013) 18–25.
[6] K. Yamaguchi, K. Ditsios, W.D. Middleton, C.F. Hildebolt, L.M. Galatz, S.A. Teefey, The demographic and morphological features of rotator cuff disease. A comparison of asymptomatic and symptomatic shoulders, J. Bone. Joint. Surg. Am. 88 (8) (2006) 1699–1704.
[7] J.A. Guevara, V. Entezari, J.C. Ho, K.A. Derwin, J.P. Iannotti, E.T. Ricchetti, An update on surgical management of the repairable large-to-massive rotator cuff tear, J. Bone. Joint. Surg. Am. 102 (19) (2020) 1742–1754.
[8] J.H. Oh, M.S. Park, S.M. Rhee, Treatment strategy for irreparable rotator cuff tears, Clin. Orthop. Surg. 10 (2) (2018) 119–134.
[9] J. Bishop, S. Klepps, I.K. Lo, J. Bird, J.N. Gladstone, E.L. Flatow, Cuff integrity after arthroscopic versus open rotator cuff repair: a prospective study, J. Shoulder Elbow Surg. 15 (3) (2006) 290–299.
[10] C. Gerber, B. Fuchs, J. Hodler, The results of repair of massive tears of the rotator cuff, J. Bone. Joint. Surg. Am. 82 (4) (2000) 505–515.
[11] Y.Y. Sun, F. Han, P. Zhang, Y.L. Zhi, J.J. Yang, X.H. Yao, et al., A synthetic bridging patch of modified co-electrospun dual nano-scaffolds for massive rotator cuff tear, J. Mater. Chem. B. 4 (45) (2016) 7259–7269.
[12] S.G. Thon, L. O'Malley 2nd, M.J. O'Brien, F.H. Savoie 3rd, Evaluation of healing rates and safety with a bioinductive collagen patch for large and massive rotator cuff tears: 2-year safety and clinical outcomes, Am. J. Sports Med. 47 (8) (2019) 1901–1908.
[13] Z. Zheng, J. Ran, W. Chen, Y. Hu, T. Zhu, X. Chen, et al., Alignment of collagen fiber in knitted silk scaffold for functional massive rotator cuff repair, Acta Biomater. 51 (2017) 317–329.
[14] W. Su, Z.Y. Wang, J. Jiang, X.Y. Liu, J.Z. Zhao, Z.J. Zhang, Promoting tendon to bone integration using graphene oxide-doped electrospun poly(lactic-co-glycolic acid) nanofibrous membrane, Int. J. Nanomed. 14 (2019) 1835–1847.
[15] X.X. Li, R.Y. Cheng, Z.Y. Sun, W. Su, G.Q. Pan, S. Zhao, et al., Flexible bipolar nanofibrous membranes for improving gradient microstructure in tendon-to-bone healing, Acta Biomater. 61 (2017) 204–216.
[16] S.J. Lee, S.H. Oh, J. Liu, S. Soker, A. Atala, J.J. Yoo, The use of thermal treatments to enhance the mechanical properties of electrospun poly(epsilon-caprolactone) scaffolds, Biomaterials 29 (10) (2008) 1422–1430.
[17] E.P. Tan, C.T. Lim, Effects of annealing on the structural and mechanical properties of electrospun polymeric nanofibres, Nanotechnology 17 (10) (2006) 2649–2654.
[18] S.X. Wang, L. Yang, L.P. Stubbs, X. Li, C. He, Lignin-derived fused electrospun carbon fibrous mats as high performance anode materials for lithium ion batteries, ACS Appl. Mater. Interfaces 5 (23) (2013) 12275–12282.
[19] M. Su, Q. Zhang, Y. Zhu, S. Wang, J. Lv, J. Sun, et al., Preparation of decellularized triphasic hierarchical bone-fibrocartilage-tendon composite extracellular matrix for enthesis regeneration, Adv. Healthc. Mater. 8 (19) (2019), e1900831.
[20] W. Liu, J. Lipner, C.H. Moran, L. Feng, X. Li, S. Thomopoulos, et al., Generation of electrospun nanofibers with controllable degrees of crimping through a simple, plasticizer-based treatment, Adv. Mater. 27 (16) (2015) 2583–2588.
[21] S.E. Szczesny, T.P. Driscoll, H.Y. Tseng, P.C. Liu, S.J. Heo, R.L. Mauck, et al., Crimped nanofibrous biomaterials mimic microstructure and mechanics of native tissue and alter strain transfer to cells, ACS Biomater. Sci. Eng. 3 (11) (2017) 2869–2876.
[22] S. Xiao, Y. Shao, B. Li, X.Q. Feng, A micromechanical model of tendon and ligament with crimped fibers, J. Mech. Behav. Biomed. Mater. 112 (2020) 104086.
[23] L. Rossetti, L.A. Kuntz, E. Kunold, J. Schock, K.W. Muller, H. Grabmayr, et al., The microstructure and micromechanics of the tendon-bone insertion, Nat. Mater. 16 (6) (2017) 664–670.
[24] Z.F. Zheng, J.S. Ran, W.S. Chen, Y.J. Hu, T. Zhu, X. Chen, et al., Alignment of collagen fiber in knitted silk scaffold for functional massive rotator cuff repair, Acta Biomater. 51 (2017) 317–329.
[25] K. Huang, W. Su, X.C. Zhang, C.A. Chen, S. Zhao, X.Y. Yan, et al., Cowpea-like Bilineage nanofiber mat for repairing chronic rotator cuff tear and inhibiting fatty infiltration, Chem. Eng. J. 392 (2019) 123671.
[26] R. Yang, G. Li, C. Zhuang, P. Yu, T. Ye, Y. Zhang, et al., Gradient bimetallic ion-based hydrogels for tissue microstructure reconstruction of tendon-to-bone insertion, Sci. Adv. 7 (26) (2021).
[27] T.H. Zhu, H.B. Gu, H.M. Zhang, H.S. Wang, H.T. Xia, X.M. Mo, et al., Covalent grafting of PEG and heparin improves biological performance of electrospun vascular grafts for carotid artery replacement, Acta Biomater. 119 (2021) 211–224.
[28] B. Zhang, X. Zhang, K. Wan, J. Zhu, J. Xu, C. Zhang, et al., Dense hydrogen-bonding network boosts ionic conductive hydrogels with extremely high toughness, rapid self-recovery, and autonomous adhesion for human-motion detection, Research 2021 (2021) 9761625.
[29] W.Y. Liu, J. Lipner, C.H. Moran, L.Z. Feng, X.Y. Li, S. Thomopoulos, et al., Generation of electrospun nanofibers with controllable degrees of crimping through a simple, plasticizer-based treatment, Adv. Mater. 27 (16) (2015) 2583–2588.
[30] J. Dulnik, P. Sajkiewicz, Crosslinking of gelatin in bicomponent electrospun fibers, Materials 14 (12) (2021).
[31] M. Bao, X.X. Lou, H.H. Yuan, Y.Z. Zhang, Electrospun biomimetic fibrous scaffold from shape memory polymer of PDLLA-co-TMC for bone tissue engineering, ACS Appl. Mater. Interfaces 6 (4) (2014) 2611–2621.
[32] H. Ebata, S. Kidoaki, Avoiding tensional equilibrium in cells migrating on a matrix with cell-scale stiffness-heterogeneity, Biomaterials 274 (2021) 120860.

[33] C.M. Madl, I.A. Flaig, C.A. Holbrook, Y.X. Wang, H.M. Blau, Biophysical matrix cues from the regenerating niche direct muscle stem cell fate in engineered microenvironments, Biomaterials 275 (2021) 120973.
[34] J. Xie, M. Bao, X. Hu, W.J.H. Koopman, W.T.S. Huck, Energy expenditure during cell spreading influences the cellular response to matrix stiffness, Biomaterials 267 (2021) 120494.
[35] K. Ye, X. Wang, L.P. Cao, S.Y. Li, Z.H. Li, L. Yu, et al., Matrix stiffness and nanoscale spatial organization of cell-adhesive ligands direct stem cell fate, Nano Lett. 15 (7) (2015) 4720–4729.
[36] R. Schipani, S. Scheurer, R. Florentin, S.E. Critchley, D.J. Kelly, Reinforcing interpenetrating network hydrogels with 3D printed polymer networks to engineer cartilage mimetic composites, Biofabrication 12 (3) (2020), 035011.
[37] J. Tang, J. Zhao, Rooting rotator cuff reconstruction for irreparable posterior-superior rotator cuff tear, Arthrosc. Tech. 10 (3) (2021) e727–e737.
[38] A. de Lima Santos, C.G. da Silva, L.S. de Sa Barreto, K.R.M. Leite, M.J.S. Tamaoki, L.M. Ferreira, et al., A new decellularized tendon scaffold for rotator cuff tears - evaluation in rabbits, BMC Muscoskel. Disord. 21 (1) (2020) 689.
[39] T. Wu, H. Li, J. Xue, X. Mo, Y. Xia, Photothermal welding, melting, and patterned expansion of nonwoven mats of polymer nanofibers for biomedical and printing applications, Angew Chem. Int. Ed. Engl. 58 (46) (2019) 16416–16421.
[40] W. Su, Z. Wang, J. Jiang, X. Liu, J. Zhao, Z. Zhang, Promoting tendon to bone integration using graphene oxide-doped electrospun poly(lactic-co-glycolic acid) nanofibrous membrane, Int. J. Nanomed. 14 (2019) 1835–1847.
[41] X. Li, R. Cheng, Z. Sun, W. Su, G. Pan, S. Zhao, et al., Flexible bipolar nanofibrous membranes for improving gradient microstructure in tendon-to-bone healing, Acta Biomater. 61 (2017) 204–216.
[42] J. Cai, J. Wang, K. Ye, D. Li, C. Ai, D. Sheng, et al., Dual-layer aligned-random nanofibrous scaffolds for improving gradient microstructure of tendon-to-bone healing in a rabbit extra-articular model, Int. J. Nanomed. 13 (2018) 3481–3492.
[43] B.D. Boyan, T.W. Hummert, D.D. Dean, Z. Schwartz, Role of material surfaces in regulating bone and cartilage cell response, Biomaterials 17 (2) (1996) 137–146.
[44] H. Miyajima, F. Ozer, S. Imazato, F.K. Mante, Surface characteristics of bioactive Ti fabricated by chemical treatment for cartilaginous-integration, Mater. Sci. Eng. C Mater. Biol. Appl. 78 (2017) 495–502.
[45] P. Weimin, L. Dan, W. Yiyong, H. Yunyu, Z. Li, Tendon-to-bone healing using an injectable calcium phosphate cement combined with bone xenograft/BMP composite, Biomaterials 34 (38) (2013) 9926–9936.
[46] Q. Liu, Y. Yu, R.L. Reisdorf, J. Qi, C.K. Lu, L.J. Berglund, et al., Engineered tendon-fibrocartilage-bone composite and bone marrow-derived mesenchymal stem cell sheet augmentation promotes rotator cuff healing in a non-weight-bearing canine model, Biomaterials 192 (2019) 189–198.
[47] V. Pandey, W. Jaap Willems, Rotator cuff tear: a detailed update, Asia Pac. J. Sports Med. Arthrosc. Rehabil. Technol. 2 (1) (2015) 1–14.
[48] C. Zhu, J. Qiu, S. Thomopoulos, Y. Xia, Augmenting tendon-to-bone repair with functionally graded scaffolds, Adv. Healthc. Mater. 10 (9) (2021), e2002269.
[49] S. Tarafder, J.A. Brito, S. Minhas, L. Effiong, S. Thomopoulos, C.H. Lee, In situ tissue engineering of the tendon-to-bone interface by endogenous stem/progenitor cells, Biofabrication 12 (1) (2019), 015008.
[50] J.T. Lyu, L. Chen, J.Q. Zhang, X. Kang, Y.J. Wang, W.J. Wu, et al., A microfluidics-derived growth factor gradient in a scaffold regulates stem cell activities for tendon-to-bone interface healing, Biomater. Sci. 8 (13) (2020) 3649–3663.
[51] D.M. Dos Santos, P.A.M. Chagas, I.S. Leite, N.M. Inada, S.R. de Annunzio, C. R. Fontana, et al., Core-sheath nanostructured chitosan-based nonwovens as a potential drug delivery system for periodontitis treatment, Int. J. Biol. Macromol. 142 (2020) 521–534.
[52] S.M.E. Zahran, A.H. Abdel-Halim, K. Nassar, A.A. Nada, Fabrication of nanofiltration membrane based on non-biofouling PVP/lecithin nanofibers reinforced with microcrystalline cellulose via needle and needle-less electrospinning techniques, Int. J. Biol. Macromol. 157 (2020) 530–543.
[53] S. Brielle, D. Bavli, A. Motzik, Y. Kan-Tor, X. Sun, C. Kozulin, et al., Delineating the heterogeneity of matrix-directed differentiation toward soft and stiff tissue lineages via single-cell profiling, Proc. Natl. Acad. Sci. U. S. A. 118 (19) (2021).
[54] Y. Long, X. Cheng, J.A. Jansen, S.G.C. Leeuwenburgh, J. Mao, F. Yang, et al., The molecular conformation of silk fibroin regulates osteogenic cell behavior by modulating the stability of the adsorbed protein-material interface, Bone Res. 9 (1) (2021) 13.
[55] Y. Yang, T. Xu, Q. Zhang, Y. Piao, H.P. Bei, X. Zhao, Biomimetic, stiff, and adhesive periosteum with osteogenic-angiogenic coupling effect for bone regeneration, Small 17 (14) (2021), e2006598.
[56] G.L. Chu, Z.Q. Yuan, C.H. Zhu, P.H. Zhou, H. Wang, W.D. Zhang, et al., Substrate stiffness- and topography-dependent differentiation of annulus fibrosus-derived stem cells is regulated by Yes-associated protein, Acta Biomater. 92 (2019) 254–264.
[57] E. Frey, F. Regenfelder, P. Sussmann, M. Zumstein, C. Gerber, W. Born, et al., Adipogenic and myogenic gene expression in rotator cuff muscle of the sheep after tendon tear, J. Orthop. Res. 27 (4) (2009) 504–509.
[58] S.K. Joshi, X. Liu, S.P. Samagh, D.H. Lovett, S.C. Bodine, H.T. Kim, et al., mTOR regulates fatty infiltration through SREBP-1 and PPARgamma after a combined massive rotator cuff tear and suprascapular nerve injury in rats, J. Orthop. Res. 31 (5) (2013) 724–730.
[59] A. Uezumi, S. Fukada, N. Yamamoto, S. Takeda, K. Tsuchida, Mesenchymal progenitors distinct from satellite cells contribute to ectopic fat cell formation in skeletal muscle, Nat. Cell Biol. 12 (2) (2010) 143–152.
[60] A. Uezumi, T. Ito, D. Morikawa, N. Shimizu, T. Yoneda, M. Segawa, et al., Fibrosis and adipogenesis originate from a common mesenchymal progenitor in skeletal muscle, J. Cell Sci. 124 (Pt 21) (2011) 3654–3664.
[61] K. Ye, X. Wang, L. Cao, S. Li, Z. Li, L. Yu, et al., Matrix stiffness and nanoscale spatial organization of cell-adhesive ligands direct stem cell fate, Nano Lett. 15 (7) (2015) 4720–4729.